24 h Evolution of an Exceptional HONO Plume Emitted by the Record-Breaking 2019/2020 Australian Wildfire Tracked from Space

Gaëlle Dufour, Maxim Eremenko, Guillaume Siour, Pasquale Sellitto, Juan Cuesta, Agnès Perrin, Matthias Beekmann

atmosphere

MDPI

Article

24 h Evolution of an Exceptional HONO Plume Emitted by the Record-Breaking 2019/2020 Australian Wildfire Tracked from Space

Gaëlle Dufour [1,*], Maxim Eremenko [2], Guillaume Siour [2], Pasquale Sellitto [2], Juan Cuesta [2], Agnès Perrin [3] and Matthias Beekmann [1]

[1] Université Paris Cité and Univ Paris Est Creteil, CNRS, LISA, F-75013 Paris, France
[2] Univ Paris Est Creteil and Université Paris Cité, CNRS, LISA, F-94010 Créteil, France
[3] LMD/IPSL, École Polytechnique, Institut Polytechnique de Paris, ENS, PSL Université, Sorbonne Université, CNRS, F-91128 Palaiseau, France
* Correspondence: gaelle.dufour@lisa.ipsl.fr

Abstract: Megafires occurred in Australia during the 2019/2020 bushfire season, leading to enhanced concentrations of many tropospheric pollutants. Here, we report on a fire plume with unusually high and persistent nitrous acid (HONO) levels that we could track during one day at free tropospheric levels over the Tasman Sea on 4 January 2020 using IASI and CrIS satellite observations. HONO concentrations up to about 25 ppb were retrieved during nighttime. Persistent HONO concentrations (>10 ppb) were still observed at sunrise, likely due to large aerosol concentrations within the plume, preventing HONO photodissociation. In addition, comparison with carbon monoxide (CO) measurements suggest a secondary production during the plume transport. Model simulations confirm that the plume is transported in the lower free troposphere with concentrations as high as 30 ppb at about 4 km. However, many uncertainties and unknowns remain in the plume aerosol load and in the chemical processes which may explain the model inability to reproduce elevated HONO concentrations at sunrise.

Keywords: nitrous acid; biomass burning; remote sensing

Citation: Dufour, G.; Eremenko, M.; Siour, G.; Sellitto, P.; Cuesta, J.; Perrin, A.; Beekmann, M. 24 h Evolution of an Exceptional HONO Plume Emitted by the Record-Breaking 2019/2020 Australian Wildfire Tracked from Space. *Atmosphere* **2022**, *13*, 1485. https://doi.org/10.3390/atmos13091485

Academic Editor: Amin Shahrokhi

Received: 17 August 2022
Accepted: 8 September 2022
Published: 13 September 2022

1. Introduction

Nitrous acid (HONO) is one of the primary sources of hydroxyl radicals (OH) by photolysis and plays a key role in tropospheric chemistry for the oxidative capacity of the atmosphere [1]. HONO primary emissions in the atmosphere come from combustion, e.g., [2] and soils [3]. Its secondary production proceeds through the gas phase reaction of NO and OH and by reactions of nitrogen-containing compounds and especially NO_2 on surfaces or on aerosols e.g., [1,2,4]. Rapid photolysis during daytime is the main HONO sink and leads to a short lifetime in the order of a ten of minutes around local noon, which limits HONO concentrations during daytime. However, large daytime HONO concentrations have already been reported by several studies, pointing at unknown or not well quantified sources, such as photo-induced heterogeneous formation, e.g., [4–7]. At night, without fast photo-dissociation, HONO tends to accumulate in the atmosphere due to light-independent heterogeneous formation on surfaces. Wildfires have a significant impact on HONO concentrations in the troposphere, e.g., [6,8,9]. However, despite aircraft and ground-based measurements being made during campaigns, e.g., [6,9,10], HONO distribution is not well-known, especially in the free troposphere, e.g., [11], compared to the near surface. Satellite detections have been reported for the IASI instrument in Australian fires in 2009 and 2019 [12,13] and an estimation of HONO volume mixing ratio (vmr) in the 2009 fire plume is provided over sea by [14]. Recently, TROPOMI has shown capabilities to cartography the HONO emitted by fires [15]. The latter study is restricted to

regions close to the sources and does not show any tracking of HONO in dispersed fire plumes over sea. It is worth noting that HONO satellite observations are mainly integrated observations with a limited capability to resolve the vertical distribution of HONO and then inform on the HONO vertical distribution. In the present study, we focus on satellite-based detection of HONO during the record-breaking 2019/2020 Australian bushfire season (also called the Australian Black Summer). These mega forest fires burnt an exceptionally large area of about 5.8 million hectares, which is more than 20% of the whole Australian temperate forests amount [16,17], destroyed more than 9000 buildings [18], and degraded air quality leading to an increase of hospitalizations and deaths [19]. This historically relevant fire season was active from September 2019 to March 2020 [20]. The concentrations of many tropospheric pollutants were enhanced in the Southern Hemisphere since the early phases of the fire season [21,22]. Furthermore, the intensity of the fires escalated and had a peak in intensity starting from New Year's Eve 2019/2020 to early January 2020 [20]. Intense events such as thunderstorms or pyrocumulonimbus clouds were generated by the bushfires [23–25]. The extreme pyro-convective clouds events led to the formation of a self-sustained smoke-charged vortex that polluted stratospheric trace gases and aerosol composition on the Hemispheric spatial scale [26].

We report here on HONO plume detection and quantification during transport at relatively high altitudes (free troposphere) using successive overpasses of four infrared (IR) sounders, i.e., CrIS and a series of IASI instruments, during the most intense phase of the 2019/2020 Australian fires in early January 2020. For the first time, HONO abundance within a plume is quantified along transport during almost 24 h after emission and its persistence was also shown during daylight hours. The CHIMERE chemistry-transport model (CTM) is used to evaluate the temporal evolution of such a plume. In Section 2, we describe the satellite instruments, the detection and retrieval methods as well as the model and simulations. In Section 3, a description of the HONO plume crossing the Tasman Sea at free tropospheric levels is given by the observations and the model. Conclusions are drawn afterwards.

2. Materials and Methods

2.1. Satellite Instruments

2.1.1. IASI

The IASI (Infrared Atmospheric Sounding Interferometer) instruments are nadir-viewing Fourier transform spectrometers [27]. Three versions of the instrument currently flew until the end of 2021 on board the EUMETSAT (European Organisation for the Exploitation of Meteorological Satellites) Metop satellites on a morning orbit (9:30LST and 21:30LST equator crossing times): one aboard the Metop-A platform since October 2006, one aboard the Metop-B platform since September 2012, and one aboard the Metop-C platform since November 2018. The IASI instruments operate in the thermal infrared (IR) between 645 and 2760 cm^{-1} with an apodized resolution of 0.5 cm^{-1} and a radiometric noise of about 0.2 K around 1000 cm^{-1}. Each IASI instrument scans the atmosphere with a swath width of 2200 km, allowing global coverage twice a day, with a field of view of 2 × 2 pixels with 12 km footprint at nadir. Metop-A, Metop-B, and Metop-C temporal difference is ~30 min.

2.1.2. CrIS

The CrIS (Cross-track Infrared Sounder) instrument is a Fourier transform spectrometer aboard the Suomi National Polar-orbiting Partnership (S-NPP) platform, in a sun-synchronous low Earth orbit with overpass times of ~01:30 and 13:30 local time. Two CrIS instruments flew, the first one since October 2011 and the second one since November 2017. In this study, we used the first of these. CrIS scans the atmosphere with a swath width of 2200 km and a field of view of 3 × 3 pixels of 14 km diameter at the nadir. CrIS is a hyperspectral infrared instrument with an unapodized spectral resolution of 0.625 cm^{-1} and low spectral noise of ~0.04 K in its long-wave infrared band 1 (648.75–1096.25 cm^{-1}) [28–30].

2.2. HONO Spectral Ratio and Retrieval Method

We use the spectral window between 785 and 795 cm^{-1} for HONO detection and retrievals (Figure 1). The spectroscopic parameters for HONO originate from a preliminary version of the linelist for the ν_4 bands of the HONO Trans- and Cis- conformers that is now available in the GEISA database [14,31]. The selected 785–795 cm^{-1} microwindow corresponds to the HONO trans-ν_4 band, where the line intensities are about 12% larger than in [14]. This is largely within the estimated accuracy associated to this entity (about 30%). Carbon dioxide and water vapor are the two main interferers in this window. Their spectroscopic data are taken from HITRAN 2004 [32].

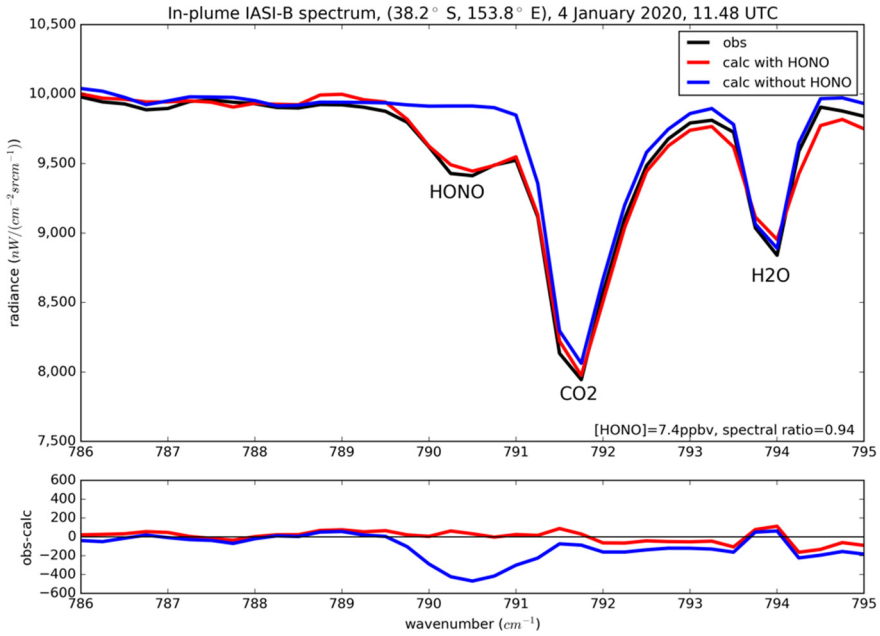

Figure 1. Example of a spectrum measured within an Australian fire plume detected on 4 January 2020 at 11.48 UTC by IASI-B. The observed spectrum (black) is compared to the direct radiative transfer calculation with (red) and without (blue) HONO included. The difference between the observed and the calculated spectra is displayed in the lower panel. The HONO contribution to the spectrum is visible between 790 and 791 cm^{-1}. H_2O and CO_2 main absorptions in the window are indicated in the figure.

HONO is a weak absorber and has been detected by IR satellite instruments only in fire plumes [12–14]. To identify fire plumes in which HONO can be observed from these instruments, a fast detection method has been developed to screen the entire satellite archives without performing time-consuming retrieval calculations. The detection is based on the spectral ratio between radiances at the wavenumber of absorption peak of the HONO trans-ν4 band and that without any HONO nor other interferers absorptions. As IASI and CrIS spectra have different spectral resolution, we use different definitions of the spectral ratio: it is the ratio between the radiances at 790.5 and 789.0 cm^{-1} for IASI and at 790.0 and 788.75 cm^{-1} for CrIS. A first threshold fixed at 0.985 is used as a first detection of the scenes and days of interest. Then, we use the distribution of the spectral ratios according to the radiance values (Figure 2) to delimit spatially the plumes. Pixels are considered within the HONO plume when their spectral ratio is smaller than the mean of the distribution minus 3σ for the corresponding radiance.

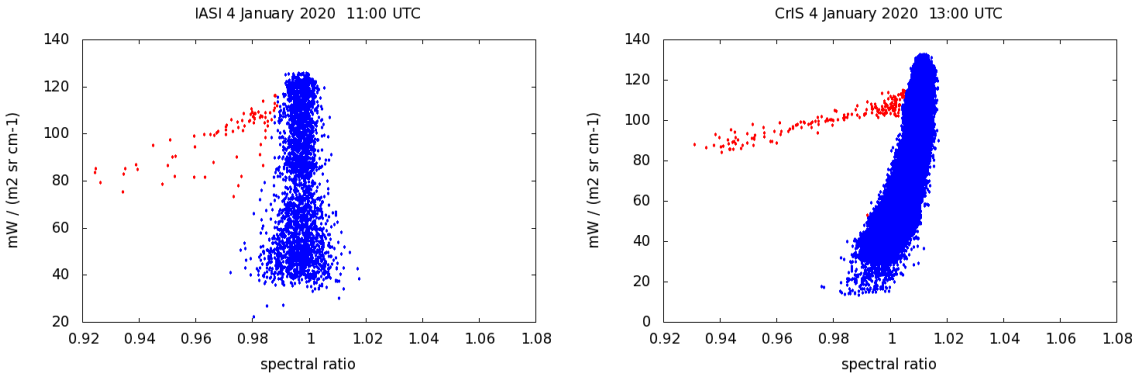

Figure 2. Examples of spectral ratio distribution for IASI (**left**) and CrIS (**right**). The pixels outside the main distribution (red) correspond to the pixels detected within the plume with the method described in the text. The blue points correspond to the pixels outside the plume.

The retrieval is performed for the pixels identified as within the plume. For these pixels, the radiative transfer (RT) is modeled using the KOPRA RT model [33] and the retrieval is performed by its inversion module, KOPRAFIT. The general framework of the retrieval is developed in [34]. The measured radiances $\boldsymbol{y}$ can be expressed as:

$$\boldsymbol{y} = F(\boldsymbol{x}) + \boldsymbol{\varepsilon} \tag{1}$$

where $\boldsymbol{x}$ is the atmospheric state, F the radiative transfer model, and $\boldsymbol{\varepsilon}$ the measurement noise.

To retrieve $\hat{\boldsymbol{x}}$, the cost function J (Equation (2)) is minimized:

$$J = (\boldsymbol{y} - F(\boldsymbol{x}))^T \mathbf{S}_\varepsilon^{-1} (\boldsymbol{y} - F(\boldsymbol{x})) + (\boldsymbol{x} - \boldsymbol{x}_a)^T \mathbf{R} (\boldsymbol{x} - \boldsymbol{x}_a) \tag{2}$$

where $\mathbf{S}_\varepsilon$ is the error covariance matrix of the measurement, $\boldsymbol{x}_a$ the a priori state vector, and $\mathbf{R}$ the regularization matrix, necessary for ill-posed inverse problems. The lack of information on the HONO variability and vertical distribution in fire plumes prevents the use of a covariance matrix for the retrieval as used in optimal estimation approaches [34]. We then employ a smoothing constraint based on the discrete first-derivative operator $\mathbf{L}_1$ as described by [35]. The constraint operator $\mathbf{R}$ is then equal to $\alpha \mathbf{L}_1^T \mathbf{L}_1$. As HONO is a weak absorber, retrieving vertical information from the spectra is not possible. We then choose to apply a strong constraint to restrict the degree of freedom in the retrieval to one (the lower limit when using $\mathbf{L}_1$ operator). The solution is then a scaled profile with the absolute scaling parameter for this profile determined by the measurement [35]. The CO_2 and H_2O absorption lines are simultaneously fitted with HONO. The choice of the a priori profile is discussed in Section 3.3 based on the results of forward trajectories simulations. Mainly, as the fire HONO plume is transported in a specific atmospheric layer, we choose to use a normalized gaussian shape for the a priori profile, center at the layer height.

2.3. Forward Trajectories Simulations

The HYSPLIT model constrained by the Global Data Assimilation System (GDAS) is used to compute forward trajectories simulations. We use the matrix calculation option of HYSPLIT. A 3 × 3 matrix centered at the fire detection location (36.5° S, 149° E) and time (4 UTC on 4 January) is used. The spatial resolution of the matrix at the starting point is 0.5°. Fourteen trajectory simulations have been done over 36 h, each of them being initialized every kilometer from 1 to 14 km. Using all the simulated trajectories, we calculate the horizontal density map of the trajectories. For that, the domain of study is gridded at a 1 × 1° resolution and we calculate the number of trajectories in each grid cell independently of the time. Similarly, we calculate the vertical distribution of the trajectories

density along the time, considering a 1 km grid on the vertical from 0 to 16 km and 1 h grid on the time.

2.4. CHIMERE

CHIMERE v2020r3 is used over a large Australian domain with a horizontal resolution of 25 × 25 km^2, extending from 56° S to 10° N and 105 to 178° E. The vertical resolution is 15 levels from the ground to 300 hPa. CHIMERE is driven by the WRF regional model version 3.7.1 [36]. A full description of WRF-CHIMERE is available in [37]. CAMS global anthropogenic v4.1 emissions [38] for the year 2019 are used. HONO anthropogenic emissions are considered as 1.5% of NOx emissions from traffic and 0.5% of NOx from other sectors. Fire emissions from CAMS GFAS [39] are considered. No diurnal cycle is applied. The injection height is calculated by the Sofiev et al. scheme [40]. We select the highest injection height parametrization for this simulation using FRP of 300 W m^{-2} and RP1 vertical profile from [41]. 80% of the mass is injected around this height and 20% from the ground to this height. NOx fire emissions are divided into 90% of NO and 10% of NO_2. The HONO gaseous chemistry is represented by MELCHIOR2 chemical mechanism described in [42]. HONO heterogeneous formation from NO_2 deposition on wet surface is considered, using the Aumont et al. formulation [2]. The different reactions (R1–R5) are listed in Table 1. In addition, the observed HONO/NO_2 ratio close to fire sources suggests that HONO primary emissions can be very high [15]. Then, we added HONO wildfire emissions as 61% of NOx emissions from GFAS. This corresponds to the upper range of HONO/NO_2 enhancement ratios observed by [15]. In addition, many studies have suggested an additional source of HONO would be present in the daytime as said before e.g., [43]. To account for this formation pathway, we added a photolytic HONO formation from heterogeneous NO_2 reaction with aerosols (R6) (Table 1). The effect of the photolysis is considered as zenithal angle function. For urban Chinese conditions, at local noon, Lu et al. (2018) derived for the collision (reactive uptake) coefficient a range of values from 1 to 8 × 10^{-4}. We retained here a collision coefficient of 10^{-3} (γ in Table 1) for solar noon, which is slightly above the upper range of these estimations and also an order of magnitude larger than the value chosen in [44] for model simulations in Beijing. The simulation includes the light independent heterogeneous HONO formation pathway.

Table 1. List of reactions involving HONO included in the CHIMERE simulations.

	Reactions	Reaction Constants	References
R1	NO + OH + M →HONO	$k = \frac{k_0[M]}{1+\frac{k_0[M]}{k_\infty}} f^p$ $p = \frac{1}{1+\left(log_{10}\left(\frac{k_0[M]}{k_\infty}\right)\right)^2}$ $k_0 = A_0 e^{\left(-\frac{B_0}{T}\right)}\left(\frac{T}{300}\right)^{-n_0}$ $k_\infty = A_\infty e^{\left(-\frac{B_\infty}{T}\right)}\left(\frac{T}{300}\right)^{-n_\infty}$ $A_0 = 7 \times 10^{-31}$, $B_0 = 0$, $n_0 = 2.6$ $A_\infty = 1.5 \times 10^{-11}$, $B_\infty = 0$, $n_\infty = 0.5$ $f = 0.6$	Atkinson et al. [45]
R2	HONO + OH →NO_2	$k(T) = Ae^{-B/T}$ $A = 1.8 \times 10^{-11}$, $B = 390$	Atkinson et al. [45]
R3	HONO + hν →NO + OH	J_{HONO}	Burkholder et al. [46]
R4	NO_2 →HONO	$ks = 0.5 \times$ depo(NO_2)	Aumont et al. [2]
R5	NO_2 →0.5 × HONO + 0.5 × HNO_3	$k_{NO2} = \frac{1}{4}\gamma\langle c\rangle S_a$ $\gamma = 5 \times 10^{-5}$	Tang et al. [47]
R6	NO_2 + hν →HONO	$k_{NO2} = \frac{1}{4}\gamma\langle c\rangle S_a max(cos(\theta_S), 0)$ $\gamma = 1 \times 10^{-3}$	Wong et al. [43]

3. Results and Discussion

3.1. HONO Detection during the Australian Black Summer

The detection procedure described in Section 2 has been applied to the entire IASI-A archive since 2007. Two main HONO detections have been found, one during the 2009 Australian fires, already reported in the literature [12,14] and one during the record-breaking Australian fires, which occurred from September 2019 to March 2020. For the latter, an intense and well-shaped plume has been detected on 4 January 2020 by the three IASI instruments and CrIS and is analyzed in detail in this study. Using combined IASI-A, IASI-B, IASI-C, and CrIS data, we are able, for the first time, to follow a HONO fire plume and the temporal evolution of HONO concentrations over a full day with several overpasses. Indeed, we can track the same plume across the Tasman Sea from Southeast Australia (South of Canberra) on 4 January 2020 04:00 UTC to West of the northern edge of New-Zealand on 5 January 2020 02:00 UTC. Figure 3 shows the HONO vmr observed during the plume transport. The HONO satellite detection occurred during the most intense phase of the 2019–2020 Australian fires, which occurred from 29 December 2019 to 4 January 2020 [17,20,24,25]. Li et al. [20] show that January 4th presents the largest fires in terms of detection counts and Fire Radiative Power (FRP) in Southeast Australia. The region of HONO detection by CrIS on January 4th at 4 UTC correspond to a temperate broadleaf and mixed forest composed mainly of eucalyptus open and woodland forest [20]. Li et al. [20] show that January 4th accounted for about 10% of seasonal biomass consumption and fire emissions. They also show that the fire emissions peak in the early afternoon between 13:00 LT (local time) and 15:00 LT, corresponding well to the time of the detection by CrIS close to 14:00 LT, local time (04:00 UTC). According to Peterson et al. [25], the detection region was marked by blow-up fires on January 4th, but without leading to pyrocumulonimbus activity which would inject fire products into the stratosphere. Then, we can expect the HONO plume detected in this study to be localized into the troposphere.

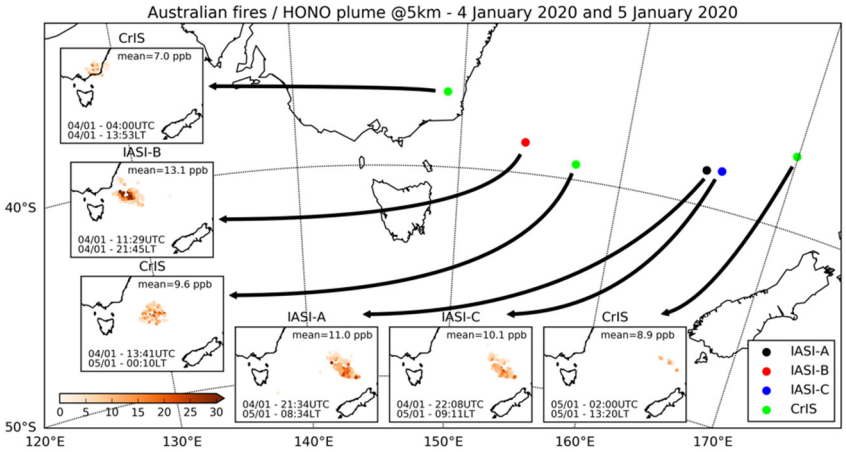

Figure 3. HONO plume tracked by CrIS and IASI instruments. The location of the center of the plume (mean latitude and longitude) is indicated in the main panel. HONO vmrs retrieved for each detection are plotted in the different subpanels. The time of the detection is indicated in UTC and Local Time (LT).

3.2. Trajectories Analysis

To evaluate the trajectory and height of the plume, we performed trajectories analysis using the HYSPLIT model, as explained in Section 2.3. The density map of all the trajectories is displayed in Figure 4. The HONO plume detected by the IASI and CrIS satellite instruments is in good spatial agreement with the airmasses trajectories for that day. We also analyze the vertical distribution of the density of trajectories to determine at which altitude the plume travels (Figure 5). A few hours after the detection by CrIS, most of the trajectories are localized between 3 and 7 km, with a maximum between 4 and 5 km. We

also check if the time of plume detection is consistent with the trajectories by calculating the mean time of the trajectories initialized between 3 and 7 km for a 1°-resolution grid in the studied area. Taking the grid cells corresponding to the center of the plume detected by each instrument, the mean trajectory times obtained are 11:48 UTC for IASI-B, 13:24 UTC for CrIS second overpass, 21:28 UTC for IASI-A, 21:53 UTC for IASI-C, and 02:40 UTC for CrIS third overpass. Trajectory times are in very good agreement with the overpass times of each instrument reported in Figure 3 (differences mainly below 30 min). This analysis demonstrates that it is well the same plume, which is sampled over 24 h by the four satellite instruments.

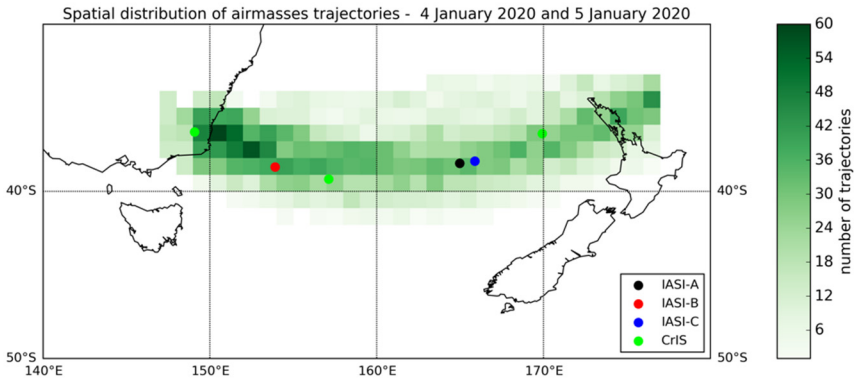

Figure 4. Density map of the trajectories initialized at 04:00 UTC on 4 January 2020 above fires (see text for details). The centers of the detected plume at different times by the satellite are indicated with colored circles.

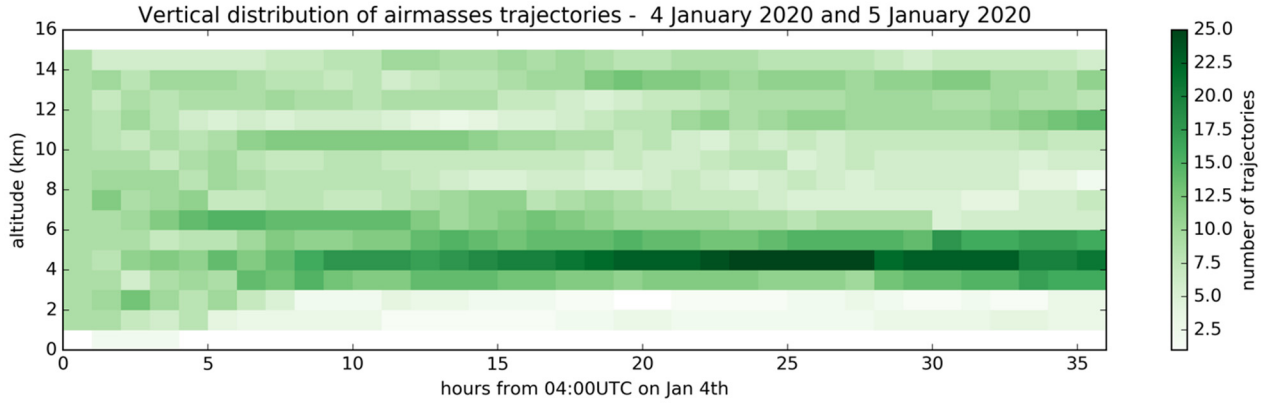

Figure 5. Density of trajectories as a function of altitude during the transport.

We also checked if the CHIMERE simulations where consistent with the trajectory analysis. The CHIMERE model simulates a HONO plume transported from Southeast Australia to New Zealand at an altitude up to about 6 km (Figure 6). More details on the simulation results are given in Section 3.4. We notice here that mixing ratios as high as 31 ppb and 16 ppb were simulated within the plume, in the lower free troposphere, at about 4 km and 5 km, respectively, during night. We use these values to define the a priori profile for the retrieval (see details in Section 3.3). Note that the plume travels over sea during night, where the boundary layer height is lower than 1 km. At the maximum activity of fire, over land, the boundary layer is much more developed, reaching almost 4 km in the model.

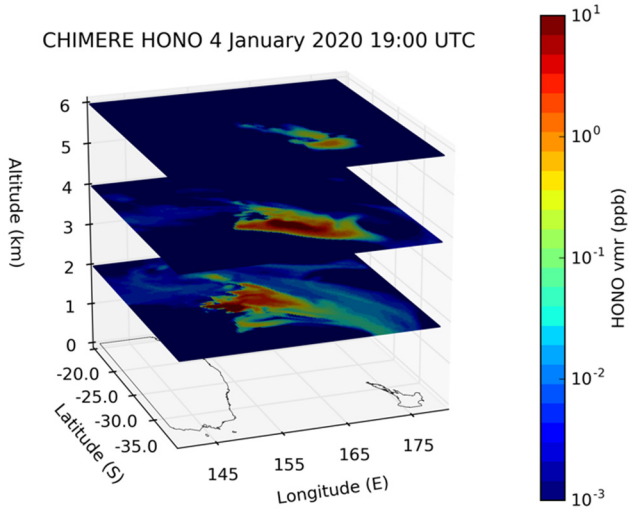

Figure 6. HONO vmrs simulated at 19:00 UTC, 4 January 2020 for different levels by CHIMERE.

3.3. HONO Retrievals Analysis

The above trajectory analysis and the CHIMERE simulations help us to define the a priori profile used for the in-plume HONO retrievals. According to the plume trajectories, most of the airmasses travel between 3 and 7 km. We choose to use a normalized gaussian shape for the a priori profile, centered at 5 km height and with a 3 km width. We multiplied the gaussian profile by 30 to have a maximum value at 5 km at 30 ppb, in the range of CHIMERE simulation. Note that our choice of using the $\mathbf{L}_1$ operator with one degree of freedom in the retrieval only constrains the shape of the profile. Choosing another maximum value for the a priori would lead to the same retrieval results. In the following, the HONO retrieved volume mixing ratio (vmr) mentioned in the text and figures correspond to the vmr at the maximum of the profile at 5 km. It is worth noting the maximum sensitivity ranges from 5 to 20 km altitude according to the averaging kernels (not shown). The retrieved HONO vmr are plotted in the subplots of Figure 3.

HONO vmr increases between 04:00 UTC (afternoon) and 11:00 UTC (night), and the sunset occurs around 06:00 UTC at these longitudes and time of the year (https://gml.noaa.gov/grad/solcalc/sunrise.html, last access 22 July 2022). Then, a slow decrease is observed from sunrise (around 15:00 UTC) onwards when HONO is photolyzed. We consider in the following the mean plume vmr as well as the 90-percentile, which is more representative of the central region of the plume where dilution with background air is reduced and the aerosol light extinction is larger, reducing HONO photolysis (during daytime) [9]. The retrieved concentrations range between 7 to 11 ppb on average, and 13.4 to 25.4 ppb in the center of the plume (90-percentile) at 5 km at the profile maximum (Table 2). Note that these vmrs are much higher than the HONO vmrs estimated in the 2009 plume by [14], which ranged from 0 to 4 ppb. In 2020, the concentrations increase during the night and reach 13.1 ppb on average, 25.4 ppb in the center of the plume at 11:30 UTC, and then start to decrease progressively when sun rises (around 15:00 UTC) and slightly drop to 8.9 ppb on average (13.4 in the center of the plume) at 02:00 UTC on 5 January 2020. This very large HONO vmr, 24 h after emissions despite sunrise, is likely explained by the large aerosol loading in the plume, which prevents HONO photolysis (see discussion later). Aerosol optical depths (AOD) larger than one were observed with MODIS in the HONO plume surroundings (Figure S2).

Table 2. HONO plume detected by CrIS and IASI instruments on 4 and 5 January 2020 between Southeast Australia and New-Zealand. The overpass time is indicated as well as the retrieved mean and 90-percentile concentrations. The values refer to the maximum of the HONO profile at 5 km.

Satellite Instrument	Date	Time (UTC)	Mean Concentration (ppb)	90-Percentile (ppb)
CrIS	4 January 2020	04:00	7.0	14.8
IASI-B	4 January 2020	11:29	13.1	25.4
CrIS	4 January 2020	13:41	9.6	18.4
IASI-A	4 January 2020	21:34	11.0	19.4
IASI-C	4 January 2020	22:08	10.1	15.3
CrIS	5 January 2020	02:00	8.9	13.4

One well-known way to estimate chemical production occurring during plume transport is to calculate the ratio of the considered species to carbon monoxide (CO). Figure S3 shows available CO satellite products at 500 hPa, measured coincidently or close in time with IASI and CrIS overpasses. We use the L3 AIRS CO product (https://airs.jpl.nasa.gov/data/get-data/standard-data, last access 18 July 2022) to compare with CrIS HONO and the IASI CO product to compare with IASI HONO (https://iasi.aeris-data.fr/, last access 22 July 2022. As shown in Figure S3, IASI CO observations are filtered out within the HONO plume due to the presence of aerosols and/or clouds. We can only derive a rough estimation of CO vmr in the vicinity of the HONO plume. Vmrs of about 600 ppb, maximum 1056 ppb are observed with IASI-B, of about 350, maximum about 700 ppb with IASI-A and IASI-C. Carbon monoxide vmrs within the plume are likely higher than these values. We use the 90th percentile of CO vmrs (825 ppb, 530 ppb, and 478 ppb respectively) to estimate an upper limit of the HONO/CO ratio determined for IASI overpasses. The AIRS L3 CO product is less filtered compared to IASI ones (Figure S3). Carbon monoxide vmrs at the center of the HONO plumes (marked with a magenta cross in Figure S3) are 335 ppb for the first (04:00 UTC) and second (13:41 UTC) CrIS overpass (04:00 UTC), and 274 ppb for the third (02:00 UTC the day after) CrIS overpass. We use these values to estimate a HONO/CO ratio for CrIS overpasses. According to the detection time, the derived HONO/CO ratio are 0.021, 0.016, 0.029, 0.021, 0.021, and 0.032. Interpreting these ratio values is difficult because (i) the CO retrievals for IASI pixels within HONO plume are rejected—our HONO/CO ratios are likely biased high when considering CO vmrs around the plumes; (ii) the AIRS CO vmrs are much smaller than the IASI ones although within the plume, likely underestimated for such intense fires. The HONO/CO is likely overestimated. This also prevents a direct comparison of the HONO/CO ratios derived from AIRS and IASI CO observations. In addition, HONO estimations are highly uncertain and dependent of the choice of the a priori profile, as discussed below. However, taking separately, the ratios calculated from AIRS (0.021, 0.029, 0.032) and IASI (0.016, 0.021, 0.021) show an increase along the transport time. This would suggest HONO production within the plume, and these results must be considered with caution.

It is worth noting that our HONO retrievals are highly uncertain as they are very sensitive to the a priori profile shape. For example, taking an altitude-constant profile would lead to smaller HONO vmr but would be similarly distributed all over the atmosphere. In that case, HONO vmr ranges between 1.3 to 2.9 ppb on average, and 2.1 to 5.5 ppb in the center of the plume (90-percentile). These differences underline the difficulties remaining in quantifying HONO vmr from IR sounders. However, our study shows interesting results: (i) the 2019/2020 Australian fires have led to a significant loading of HONO in fire plume on 4 January (vmr in the range 1–10 ppb in the free troposphere), even if it is difficult to quantify precisely, (ii) the persistence of large HONO vmr during 24 h, and the photolysis of HONO being strongly reduced by aerosols and clouds, (iii) the production of HONO during plume transport.

3.4. Comparison with Model Simulations

We use the CTM CHIMERE to simulate HONO in the 2019/2020 Australian fires as described in Section 2.4. Simulating correct HONO concentrations is a great challenge for models due to the large uncertainties in the fire emissions (location, intensity, emission factors, injection height etc), their HONO fraction, and plume chemistry, particularly heterogeneous HONO formation, photo-induced or not. CHIMERE simulations are then used to evaluate mainly the HONO temporal evolution within the fire plume rather than absolute concentrations. For 4 January 2020, the model simulates a HONO plume as the one detected by the satellite instruments. The simulated plume starts in the vicinity of Sydney, northward compared to the observed plume, which is detected southward to Canberra (Figure 7). It is worth noting that emissions used by the model cover the regions from Sydney southward to the Australian southern coast, but large uplifted HONO concentrations are simulated only in the northern part of the emission region, despite state-of-the-art vertical mixing scheme in the model [48]. The simulated plume extends up to the level 12 of the model, between 6 and 7 km. The upper part of the plume moves faster and further away above the Tasman Sea towards the western part of New Zealand (Figure 6). Due to the vertical sensitivity of IR sounders and the forward trajectories analysis, we focus on the model levels around 4 and 5 km altitude.

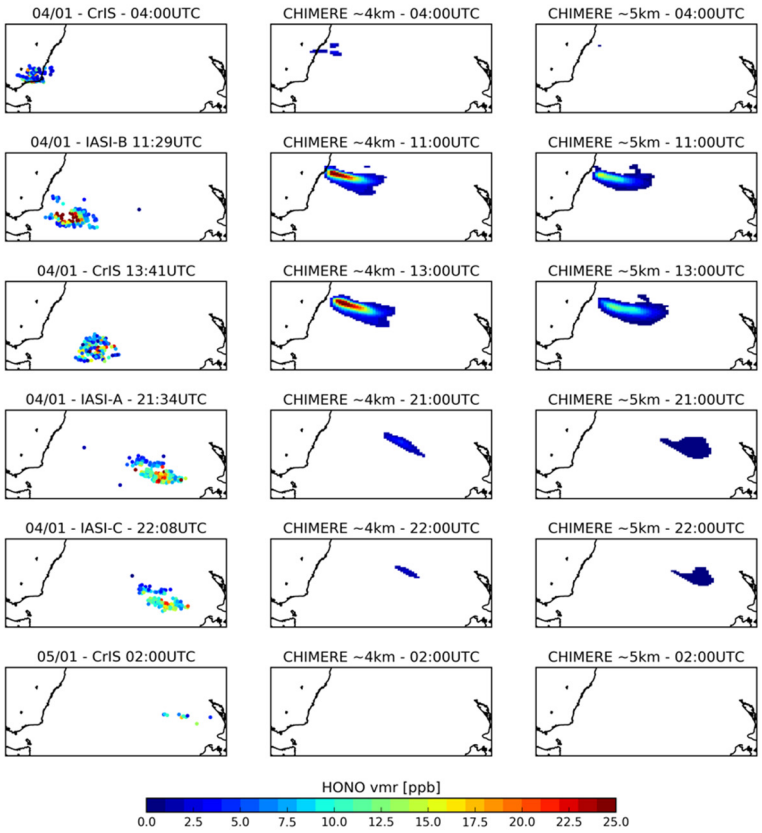

Figure 7. Observed and simulated (~4 and ~5 km) HONO vmrs within the plume around the detection times.

To delimit the plume, we fixed a threshold at 1 ppb for level 10 (~4 km) of the model, and at 0.5 ppb for level 11 (~5 km), except for 04:00 UTC, 21:00 UTC, 22:00 UTC, and 23:00 UTC, where the threshold is fixed at 0.2 ppb (Figure 7). The temporal evolution of the 90th percentiles of plume concentrations during 4 January is plotted in Figure 8. At the first detection by the satellite at 04:00 UTC, the simulated HONO plume is visible only up to level 10 (~4 km). It starts to be visible one hour later at level 11. At 4 km, HONO vmrs within the center of the plume (90th percentile) increase from 2.5 ppb at 04:00 UTC to reach a maximum around 17–18 ppb during night between 10:00 UTC and 14:00 UTC.

At sunrise (around 15:00 UTC), HONO vmrs decreases progressively down to few ppb. At 5 km, the maximum HONO vmrs (~10 ppb) are simulated during a sharper period (11:00–12:00 UTC). The decrease is then slower than at 4 km. HONO vmrs drop abruptly at 20:00 UTC. By comparison, satellite observations show a maximum (25 ppb) at 11:00 UTC follow by a drop at 13:41 UTC. This temporal evolution is in relative agreement with the simulation at 5 km. However, it is worth noting that the observed HONO vmrs remain large well after the sunrise suggesting either that the aerosol loading within the plume is large enough to strongly limit the HONO photolysis or that chemical processes compensate HONO photolysis. Concerning HONO photodissociation, the aerosol induced actinic flux attenuation is included in the model, but the photodissociation rate may be biased high, if aerosol mass is biased low. It would have been interesting to evaluate the simulated aerosol mass within the plume using AOD observations. However, it is difficult because the model plume is not well coincident with the observed plume, and MODIS AODs are contaminated by clouds in most of the plume and then filtered (Figure S2). Another process, which may contribute to faster HONO decrease in the model, is the dilution of the plume. It certainly plays a role in reducing HONO levels, but this process is expected to happen continuously and not only at sunrise. Another hypothesis to explain less persistent plume simulated by the model is the uncertainty on the photoinduced collision coefficient (R6). We fixed it to 10^{-3} (at cloud free local noon), at the upper end of values given in the available literature (10^{-4}–10^{-3} as discussed in Section 2.4), but it might still be underestimated. Alternatively or in addition, available aerosol surface might be higher than estimated by our model assuming spherical particles. For example, fire aerosol can be highly porous through the formation of soot aggregates [49]. These hypotheses warrant for further studies. It is also worth noting that, according to chemical tracers studies with the model (not shown), the main contributions to HONO in the plume are the photo-induced heterogeneous reaction (R6, Table 1), the light independent heterogeneous reaction (R5, Table 1), and the primary fire emissions. Other sources, such as anthropogenic ones are negligeable.

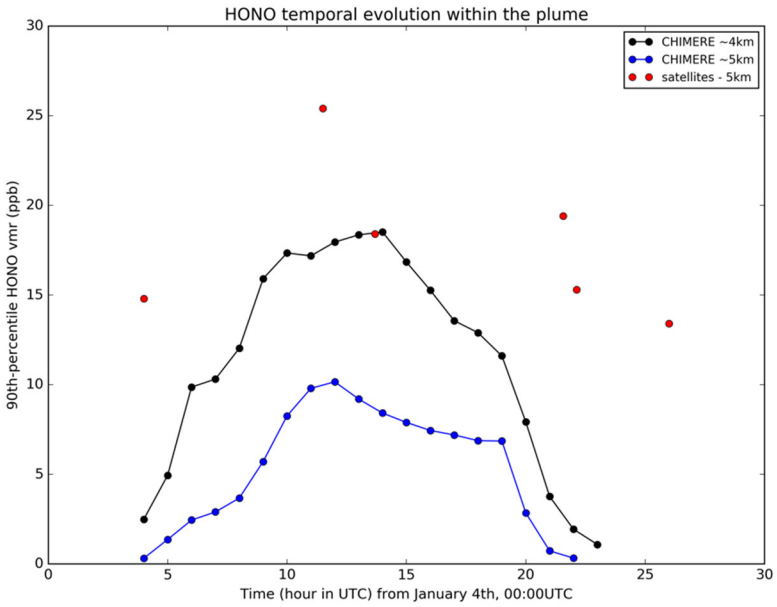

Figure 8. Temporal evolution of HONO simulated at ~4 km (black) and ~5 km (blue) by CHIMERE and observed by satellite instruments. The vmrs correspond to the 90th-percentile of the HONO vmr within the plume.

We also evaluate the HONO/CO ratio within the simulated plume. The mean CO vmrs at 5 km range 750 to 1260 ppb in relatively good agreement with CO observed with IASI, but larger than those from AIRS. As the mean HONO vmrs simulated by the model are smaller than the ones measured by satellite, this leads to HONO/CO ratios almost one

order of magnitude smaller than the ones derived from observations. For 4 January, they move from 0.0004 at 04:00 UTC to about 0.003 during night (11:00 and 13:00 UTC) and drop 0.0002 at 22:00 UTC (note that no HONO plume is simulated at 5 km on 5 January). Despite the difference in magnitude for the ratio, we can notice the simulated ratio increases during night as the observed night also suggesting a nighttime production of HONO. The behavior of the simulated and observed ratio differs when sun rises as the HONO photolysis is likely too fast in the model for the plume conditions.

4. Conclusions

Satellite infrared sounders, trajectory analysis, and chemical transport model simulations are used to study 2019/2020 Australian fires, in particular their consequences on atmospheric HONO concentrations. For the first time, a HONO plume emitted by these record-breaking fires has been tracked, and its evolution quantified during one day above the Tasman Sea by four satellite instruments, the three IASI, and CrIS. HONO vmrs of several ppb have been retrieved within the plume. The remarkable points rise from the transport at free tropospheric altitudes of the plumes and the persistence of large HONO vmr (>10 ppb) after one day during sunrise, likely due to a large aerosol loading within the plume, which prevents HONO photodissociation. The HONO/CO ratio would suggest HONO production within the plume in addition to primary emissions. Model simulations, aiming at reproducing partly this exceptional event, confirm that the plume is transported in the free troposphere. It is more difficult to identify which processes explain the observed HONO vmrs due to large uncertainties in both simulations and observations. In particular, the question of the processes involved to explain the persistent HONO concentrations at sunrise is not resolved at that stage, the model showing a much stronger decrease of HONO when the sun rises, which points to remaining unknowns in chemistry and aerosol loading in the plume.

Supplementary Materials: The following supporting information can be downloaded at: https://www.mdpi.com/article/10.3390/atmos13091485/s1, Figure S1: HONO vmrs simulated at 04:00 UTC, 11:00 UTC, 14:00 UTC and 22:00 UTC on 4 January 2020 for different levels by CHIMERE. Figure S2: MODIS AOD observed close to the CrIS HONO detection time. The cross indicates the center of the detected HONO plume. The time evolution of the AOD averaged over a region $+/-2^{\circ}$ around the center of HONO plume is displayed in the lower right panel. Figure S3: Carbon monoxide vmrs retrieved at 500 hPa by AIRS (daily L3 product) and IASI instruments coincident or close in time with the HONO plume detection by CrIS and IASI reported in Figure 3. The ascending overpass of AIRS corresponds to the daytime CrIS observations (at 4:00 UTC on 4 Januray and at 2 UTC on 5 January). The descending overpass corresponds to the nighttime CrIS observations (at about 13:30 UTC). The center of the HONO plume is indicated by a magenta cross on each subplot.

Author Contributions: Conceptualization, G.D. and M.E.; methodology, G.D. and M.E.; software, M.E. and G.S.; formal analysis, G.D., M.E. and J.C.; investigation, G.D., M.E., G.S. and M.B.; resources, A.P.; data curation, M.E., G.S. and A.P.; writing—original draft preparation, G.D., G.S., P.S., J.C., M.B. and A.P.; visualization, G.D.; supervision, G.D.; project administration, G.D.; funding acquisition, G.D. All authors have read and agreed to the published version of the manuscript.

Funding: This research was funded by CNES, grants IASI/TOSCA and IASI-NG/TOSCA.

Data Availability Statement: The IASI Level 1C data used for the HONO observations in fire plumes in the study are available at the French Data and Service for the Atmosphere (AERIS) portal via https://iasi.aeris-data.fr/ (Last access date: 12 September 2022) with registration. The CrIS Level 1 data used for the HONO observations in fire plumes in the study are available at the GES DISC NASA portal via https://sounder.gesdisc.eosdis.nasa.gov/data/SNPP_Sounder_Level1/SNPPCrISL1BNSR.2/ (Last access date: 12 September 2022) with registration. The AIRS CO Level 3 data are available also at the GES DISC NASA portal (https://disc.gsfc.nasa.gov/ (Last access date: 12 September 2022). V2020r3 of the CHIMERE model used for simulating HONO in Australian fire is available via the GNU General Public License with registration and developed openly at https://www.lmd.polytechnique.fr/chimere/ (Last access date: 12 September 2022). The emission inventory data used for the HONO simulations as input of the CHIMERE model are available at

the French Data and Service for the Atmosphere (AERIS) portal via https://eccad.aeris-data.fr/ (Last access date: 12 September 2022) with registration. Version 5.1.0 of the HYSPLIT transport and dispersion model used to calculate trajectories of fire plumes in this study is preserved at https://www.ready.noaa.gov (Last access date: 12 September 2022), available openly through the website and developed openly at https://www.ready.noaa.gov (Last access date: 12 September 2022).

Acknowledgments: The authors acknowledge the different data centers to make satellite and emission data available: the Data and Service for the Atmosphere (AERIS) portal and the NASA GESDISC system. The authors gratefully acknowledge the NOAA Air Resources Laboratory (ARL) for the provision of the HYSPLIT model and/or READY website used in this publication. We acknowledge the Institut für Meteorologie und Klimaforschung (IMK), Karlsruhe, Germany, for a licence to use the KOPRA radiative transfer model. This work was granted access to the HPC resources of TGCC under the allocations A0070107232 and A0090107232. The IASI mission is a joint mission of EUMETSAT and the Centre National d'Etudes Spatiales (CNES, France).

Conflicts of Interest: The authors declare no conflict of interest.

References

1. Finlayson-Pitts, B.; Pitts, J., Jr. *Chemistry of the Upper and Lower Atmosphere*, 1st ed.; Academic Press: Cambridge, MA, USA, 1999; ISBN 978-0-12-257060-5.
2. Aumont, B.; Chervier, F.; Laval, S. Contribution of HONO Sources to the NOx/HOx/O3 Chemistry in the Polluted Boundary Layer. *Atmos. Environ.* **2003**, *37*, 487–498. [CrossRef]
3. Stemmler, K.; Ammann, M.; Donders, C.; Kleffmann, J.; George, C. Photosensitized Reduction of Nitrogen Dioxide on Humic Acid as a Source of Nitrous Acid. *Nature* **2006**, *440*, 195–198. [CrossRef] [PubMed]
4. Kleffmann, J. Daytime Sources of Nitrous Acid (HONO) in the Atmospheric Boundary Layer. *ChemPhysChem* **2007**, *8*, 1137–1144. [CrossRef] [PubMed]
5. Lu, X.; Wang, Y.; Li, J.; Shen, L.; Fung, J.C.H. Evidence of Heterogeneous HONO Formation from Aerosols and the Regional Photochemical Impact of This HONO Source. *Environ. Res. Lett.* **2018**, *13*, 114002. [CrossRef]
6. Neuman, J.A.; Trainer, M.; Brown, S.S.; Min, K.-E.; Nowak, J.B.; Parrish, D.D.; Peischl, J.; Pollack, I.B.; Roberts, J.M.; Ryerson, T.B.; et al. HONO Emission and Production Determined from Airborne Measurements over the Southeast U.S. *J. Geophys. Res. Atmos.* **2016**, *121*, 9237–9250. [CrossRef]
7. Michoud, V.; Colomb, A.; Borbon, A.; Miet, K.; Beekmann, M.; Camredon, M.; Aumont, B.; Perrier, S.; Zapf, P.; Siour, G.; et al. Study of the Unknown HONO Daytime Source at a European Suburban Site during the MEGAPOLI Summer and Winter Field Campaigns. *Atmos. Chem. Phys.* **2014**, *14*, 2805–2822. [CrossRef]
8. Akagi, S.K.; Yokelson, R.J.; Wiedinmyer, C.; Alvarado, M.J.; Reid, J.S.; Karl, T.; Crounse, J.D.; Wennberg, P.O. Emission Factors for Open and Domestic Biomass Burning for Use in Atmospheric Models. *Atmos. Chem. Phys.* **2011**, *11*, 4039–4072. [CrossRef]
9. Peng, Q.; Palm, B.B.; Melander, K.E.; Lee, B.H.; Hall, S.R.; Ullmann, K.; Campos, T.; Weinheimer, A.J.; Apel, E.C.; Hornbrook, R.S.; et al. HONO Emissions from Western U.S. Wildfires Provide Dominant Radical Source in Fresh Wildfire Smoke. *Environ. Sci. Technol.* **2020**, *54*, 5954–5963. [CrossRef]
10. Bourgeois, I.; Peischl, J.; Neuman, J.A.; Brown, S.S.; Allen, H.M.; Campuzano-Jost, P.; Coggon, M.M.; DiGangi, J.P.; Diskin, G.S.; Gilman, J.B.; et al. Comparison of Airborne Measurements of NO, NO_2, HONO, NO_y and CO during FIREX-AQ. *Atmos. Meas. Tech. Discuss.* **2022**, *15*, 4901–4930. [CrossRef]
11. Kleffmann, J.; Wiesen, P. Technical Note: Quantification of Interferences of Wet Chemical HONO LOPAP Measurements under Simulated Polar Conditions. *Atmos. Chem. Phys.* **2008**, *8*, 6813–6822. [CrossRef]
12. Clarisse, L.; R'Honi, Y.; Coheur, P.F.; Hurtmans, D.; Clerbaux, C. Thermal Infrared Nadir Observations of 24 Atmospheric Gases. *Geophys. Res. Lett.* **2011**, *38*, L10802. [CrossRef]
13. Longueville, H.D.; Clarisse, L.; Whitburn, S.; Franco, B.; Bauduin, S.; Clerbaux, C.; Camy-Peyret, C.; Coheur, P.-F. Identification of Short and Long-Lived Atmospheric Trace Gases from IASI Space Observations. *Geophys. Res. Lett.* **2021**, *48*, e2020GL091742. [CrossRef]
14. Armante, R.; Perrin, A.; Kwabia Tchana, F.; Manceron, L. The N4 Bands at 11 Mm: Linelists for the Trans- and Cis- Conformer Forms of Nitrous Acid (HONO) in the 2019 Version of the GEISA Database*. *Mol. Phys.* **2021**, e1951860. [CrossRef]
15. Theys, N.; Volkamer, R.; Müller, J.-F.; Zarzana, K.J.; Kille, N.; Clarisse, L.; De Smedt, I.; Lerot, C.; Finkenzeller, H.; Hendrick, F.; et al. Global Nitrous Acid Emissions and Levels of Regional Oxidants Enhanced by Wildfires. *Nat. Geosci.* **2020**, *13*, 681–686. [CrossRef]
16. Boer, M.M.; Resco de Dios, V.; Bradstock, R.A. Unprecedented Burn Area of Australian Mega Forest Fires. *Nat. Clim. Chang.* **2020**, *10*, 171–172. [CrossRef]
17. Bowman, D.; Williamson, G.; Yebra, M.; Lizundia-Loiola, J.; Pettinari, M.L.; Shah, S.; Bradstock, R.; Chuvieco, E. Wildfires: Australia Needs National Monitoring Agency. *Nature* **2020**, *584*, 188–191. [CrossRef]
18. Filkov, A.I.; Ngo, T.; Matthews, S.; Telfer, S.; Penman, T.D. Impact of Australia's Catastrophic 2019/20 Bushfire Season on Communities and Environment. Retrospective Analysis and Current Trends. *J. Saf. Sci. Resil.* **2020**, *1*, 44–56. [CrossRef]

19. Johnston, F.H.; Borchers-Arriagada, N.; Morgan, G.G.; Jalaludin, B.; Palmer, A.J.; Williamson, G.J.; Bowman, D.M.J.S. Unprecedented Health Costs of Smoke-Related PM2.5 from the 2019–20 Australian Megafires. *Nat. Sustain.* **2021**, *4*, 42–47. [CrossRef]
20. Li, F.; Zhang, X.; Kondragunta, S. Highly Anomalous Fire Emissions from the 2019–2020 Australian Bushfires. *Environ. Res. Commun.* **2021**, *3*, 105005. [CrossRef]
21. Kloss, C.; Sellitto, P.; von Hobe, M.; Berthet, G.; Smale, D.; Krysztofiak, G.; Xue, C.; Qiu, C.; Jégou, F.; Ouerghemmi, I.; et al. Australian Fires 2019–2020: Tropospheric and Stratospheric Pollution Throughout the Whole Fire Season. *Front. Environ. Sci.* **2021**, *9*, 220. [CrossRef]
22. Pope, R.J.; Kerridge, B.J.; Siddans, R.; Latter, B.G.; Chipperfield, M.P.; Arnold, S.R.; Ventress, L.J.; Pimlott, M.A.; Graham, A.M.; Knappett, D.S.; et al. Large Enhancements in Southern Hemisphere Satellite-Observed Trace Gases Due to the 2019/2020 Australian Wildfires. *J. Geophys. Res. Atmos.* **2021**, *126*, e2021JD034892. [CrossRef]
23. Bowman, D.M.J.S.; Kolden, C.A.; Abatzoglou, J.T.; Johnston, F.H.; van der Werf, G.R.; Flannigan, M. Vegetation Fires in the Anthropocene. *Nat. Rev. Earth Environ.* **2020**, *1*, 500–515. [CrossRef]
24. Kablick III, G.P.; Allen, D.R.; Fromm, M.D.; Nedoluha, G.E. Australian PyroCb Smoke Generates Synoptic-Scale Stratospheric Anticyclones. *Geophys. Res. Lett.* **2020**, *47*, e2020GL088101. [CrossRef]
25. Peterson, D.A.; Fromm, M.D.; McRae, R.H.D.; Campbell, J.R.; Hyer, E.J.; Taha, G.; Camacho, C.P.; Kablick, G.P.; Schmidt, C.C.; DeLand, M.T. Australia's Black Summer Pyrocumulonimbus Super Outbreak Reveals Potential for Increasingly Extreme Stratospheric Smoke Events. *npj Clim. Atmos. Sci.* **2021**, *4*, 38. [CrossRef]
26. Sellitto, P.; Belhadji, R.; Kloss, C.; Legras, B. Radiative impacts of the Australian bushfires 2019–2020—Part 1: Large-scale radiative forcing. *Atmos. Chem. Phys.* **2022**, *22*, 9299–9311. [CrossRef]
27. Clerbaux, C.; Boynard, A.; Clarisse, L.; George, M.; Hadji-Lazaro, J.; Herbin, H.; Hurtmans, D.; Pommier, M.; Razavi, A.; Turquety, S.; et al. Monitoring of Atmospheric Composition Using the Thermal Infrared IASI/MetOp Sounder. *Atmos. Chem. Phys.* **2009**, *9*, 6041–6054. [CrossRef]
28. Han, Y.; Revercomb, H.; Cromp, M.; Gu, D.; Johnson, D.; Mooney, D.; Scott, D.; Strow, L.; Bingham, G.; Borg, L.; et al. Suomi NPP CrIS Measurements, Sensor Data Record Algorithm, Calibration and Validation Activities, and Record Data Quality. *J. Geophys. Res. Atmos.* **2013**, *118*, 12734–12748. [CrossRef]
29. Strow, L.L.; Motteler, H.; Tobin, D.; Revercomb, H.; Hannon, S.; Buijs, H.; Predina, J.; Suwinski, L.; Glumb, R. Spectral Calibration and Validation of the Cross-Track Infrared Sounder on the Suomi NPP Satellite. *J. Geophys. Res. Atmos.* **2013**, *118*, 12486–12496. [CrossRef]
30. Tobin, D.; Revercomb, H.; Knuteson, R.; Taylor, J.; Best, F.; Borg, L.; DeSlover, D.; Martin, G.; Buijs, H.; Esplin, M.; et al. Suomi-NPP CrIS Radiometric Calibration Uncertainty. *J. Geophys. Res. Atmos.* **2013**, *118*, 10589–10600. [CrossRef]
31. Delahaye, T.; Armante, R.; Scott, N.A.; Jacquinet-Husson, N.; Chédin, A.; Crépeau, L.; Crevoisier, C.; Douet, V.; Perrin, A.; Barbe, A.; et al. The 2020 Edition of the GEISA Spectroscopic Database. *J. Mol. Spectrosc.* **2021**, *380*, 111510. [CrossRef]
32. Rothman, L.S.; Jacquemart, D.; Barbe, A.; Benner, D.C.; Birk, M.; Brown, L.R.; Carleer, M.R.; Chackerian, C., Jr.; Chance, K.; Coudert, L.H.; et al. The HITRAN 2004 Molecular Spectroscopic Database. *J. Quant. Spectrosc. Radiat. Transfer* **2005**, *96*, 139–204. [CrossRef]
33. Stiller, G.P.; von Clarmann, T.; Dudhia, A.; Echle, G.; Funke, B.; Glatthor, N.; Hase, F.; Höpfner, M.; Kellmann, S.; Kemnitzer, H.; et al. *The Karlsruhe Optimized and Precise Radiative Transfer Algorithm (KOPRA), Vol. FZKA 6487 of Wissenschaftliche Berichte*; Stiller, G.P., Ed.; Forschungszentrum: Karlsruhe, Germany, 2000.
34. Rodgers, C.D. *Inverse Methods for Atmospheric Sounding: Theory and Practice*; World Scientific: Singapore, 2000; Volume 2.
35. Steck, T. Methods for Determining Regularization for Atmospheric Retrieval Problems. *Appl. Opt. AO* **2002**, *41*, 1788–1797. [CrossRef] [PubMed]
36. Skamarock, W.; Klemp, J.; Dudhia, J.; Gill, D.; Barker, D.; Wang, W.; Huang, X.-Y.; Duda, M. A Description of the Advanced Research WRF Version 3; UCAR/NCAR (Boulder, Colorado, US): 2008; p. 1002 KB. UCAR/NCAR: Boulder, CO, USA, 2008; p. 1002 KB.
37. Menut, L.; Bessagnet, B.; Briant, R.; Cholakian, A.; Couvidat, F.; Mailler, S.; Pennel, R.; Siour, G.; Tuccella, P.; Turquety, S.; et al. The CHIMERE V2020r1 Online Chemistry-Transport Model. *Geosci. Model Dev. Discuss.* **2021**, *14*, 6781–6811. [CrossRef]
38. Granier, C.; Darras, S.; Denier van der Gon, H.; Doubalova, J.; Elguindi, N.; Galle, B.; Gauss, M.; Guevara, M.; Jalkanen, J.-P.; Kuenen, J.; et al. *The Copernicus Atmosphere Monitoring Service Global and Regional Emissions (April 2019 Version)*; Copernicus Atmosphere Monitoring Service (CAMS) report; 2019. [CrossRef]
39. Kaiser, J.W.; Heil, A.; Andreae, M.O.; Benedetti, A.; Chubarova, N.; Jones, L.; Morcrette, J.-J.; Razinger, M.; Schultz, M.G.; Suttie, M.; et al. Biomass Burning Emissions Estimated with a Global Fire Assimilation System Based on Observed Fire Radiative Power. *Biogeosciences* **2012**, *9*, 527–554. [CrossRef]
40. Sofiev, M.; Ermakova, T.; Vankevich, R. Evaluation of the Smoke-Injection Height from Wild-Land Fires Using Remote-Sensing Data. *Atmos. Chem. Phys.* **2012**, *12*, 1995–2006. [CrossRef]
41. Menut, L.; Flamant, C.; Turquety, S.; Deroubaix, A.; Chazette, P.; Meynadier, R. Impact of Biomass Burning on Pollutant Surface Concentrations in Megacities of the Gulf of Guinea. *Atmos. Chem. Phys.* **2018**, *18*, 2687–2707. [CrossRef]
42. Menut, L.; Bessagnet, B.; Khvorostyanov, D.; Beekmann, M.; Blond, N.; Colette, A.; Coll, I.; Curci, G.; Foret, G.; Hodzic, A.; et al. CHIMERE 2013: A Model for Regional Atmospheric Composition Modelling. *Geosci. Model Dev.* **2013**, *6*, 981–1028. [CrossRef]

43. Wong, K.W.; Tsai, C.; Lefer, B.; Grossberg, N.; Stutz, J. Modeling of Daytime HONO Vertical Gradients during SHARP 2009. *Atmos. Chem. Phys.* **2013**, *13*, 3587–3601. [CrossRef]
44. Liu, J.; Liu, Z.; Ma, Z.; Yang, S.; Yao, D.; Zhao, S.; Hu, B.; Tang, G.; Sun, J.; Cheng, M.; et al. Detailed Budget Analysis of HONO in Beijing, China: Implication on Atmosphere Oxidation Capacity in Polluted Megacity. *Atmos. Environ.* **2021**, *244*, 117957. [CrossRef]
45. Atkinson, R.; Baulch, D.L.; Cox, R.A.; Hampson, J.; Kerr, J.A.C.; Rossi, M.J.; Troe, J. Evaluated Kinetic, Photochemical and Heterogeneous Data for Atmospheric Chemistry: Supplement V, IUPAC Subcommittee on Gas Kinetic Data Evaluation for Atmospheric Chemistry. *J. Phys. Chem. Ref. Data* **1997**, *26*, 521–1011. [CrossRef]
46. Burkholder, J.B.; Sander, S.P.; Abbat, J.; Barker, J.R.; Huie, R.E.; Kolb, C.E.; Kurylo, M.J.; Orkin, V.L.; Wilmouth, D.M.; Wine, P.H. *Chemical Kinetics and Photochemical Data for Use in Atmospheric Studies*; Jet Propulsion Laboratory: Pasadena, CA, USA, 2015.
47. Tang, Y.; An, J.; Li, Y.; Wang, F. Uncertainty in the Uptake Coefficient for HONO Formation on Soot and Its Impacts on Concentrations of Major Chemical Components in the Beijing–Tianjin–Hebei Region. *Atmos. Environ.* **2014**, *84*, 163–171. [CrossRef]
48. Lachatre, M.; Mailler, S.; Menut, L.; Turquety, S.; Sellitto, P.; Guermazi, H.; Salerno, G.; Caltabiano, T.; Carboni, E. New Strategies for Vertical Transport in Chemistry Transport Models: Application to the Case of the Mount Etna Eruption on 18 March 2012 with CHIMERE V2017r4. *Geosci. Model Dev.* **2020**, *13*, 5707–5723. [CrossRef]
49. Chakrabarty, R.K.; Beres, N.D.; Moosmüller, H.; China, S.; Mazzoleni, C.; Dubey, M.K.; Liu, L.; Mishchenko, M.I. Soot Superaggregates from Flaming Wildfires and Their Direct Radiative Forcing. *Sci. Rep.* **2014**, *4*, 5508. [CrossRef] [PubMed]